Synchrotron-based far-infrared spectroscopy of HC3N: Extended ro-vibrational analysis and new line list up to 3360 cm−1

19 September 2024

Synchrotron-based far-infrared spectroscopy of HC_3N: extended ro-vibrational analysis and new line list up to 3360 cm^{-1}

Filippo Tamassia[a,*], Luca Bizzocchi[b,c,*], Mattia Melosso[c,*], Marie-Aline Martin-Drumel[d], Olivier Pirali[d,e], Andrea Pietropolli Charmet[f], Elisabetta Canè[a], Luca Dore[c], Iouli E. Gordon[g], Jean-Claude Guillemin[h], Barbara M. Giuliano[i], Paola Caselli[i], Silvia Alessandrini[b,c], Vincenzo Barone[b], Cristina Puzzarini[c]

[a]*Dipartimento di Chimica Industriale "Toso Montanari", Università di Bologna, Viale del Risorgimento 4, 40136 Bologna, Italy*
[b]*Scuola Normale Superiore, Piazza dei Cavalieri 7, 56126 Pisa, Italy*
[c]*Dipartimento di Chimica "Giacomo Ciamician", Università di Bologna, Via F. Selmi 2, 40126 Bologna, Italy*
[d]*Université Paris-Saclay, CNRS, Institut des Sciences Moléculaires d'Orsay, 91405 Orsay, France*
[e]*SOLEIL Synchrotron, AILES beamline, l'Orme des Merisiers, Saint-Aubin, 91190 Gif-sur-Yvette, France*
[f]*Dipartimento di Scienze Molecolari e Nanosistemi, Università Ca' Foscari Venezia, Via Torino 155, 30172 Mestre, Italy*
[g]*Harvard-Smithsonian Center for Astrophysics, Atomic and Molecular Physics Division, Cambridge, MA, USA*
[h]*Université de Rennes, Ecole Nationale Supérieure de Chimie de Rennes, CNRS, ISCR–UMR6226, 35000 Rennes, France*
[i]*Center for Astrochemical Studies, Max Planck Institut für extraterrestrische Physik Gießenbachstraße 1, 85748 Garching bei München, Germany*

Abstract

The far-infrared spectrum of HC_3N has been recorded at high resolution between 70 and 500 cm^{-1} using synchrotron radiation. Four prominent features, i.e., ν_7, $\nu_6 - \nu_7$, $\nu_4 - \nu_6$, and $2\nu_7$ have been identified in the spectrum together with many associated hot bands. In addition, rotational transitions for the interacting $v_4 = v_7 = 1$, $(v_6 = 2, v_7 = 1)$, $(v_5 = 1, v_7 = 2)$, and $v_7 = 5$ vibrationally excited states have been recorded in the millimeter/submillimeter region. The newly assigned transitions, together with those reported previously, form a comprehensive data set including about 17 000 transitions, which involves almost all the vibrational states of HC_3N lying below 1300 cm^{-1} plus some excited states with energies between 2075 and 3550 cm^{-1}. These data have been fitted to an effective Hamiltonian which takes into account rotational and vibrational l-type resonance effects, together with a number of anharmonic interaction terms. On average, all the analysed data are reproduced within the experimental accuracy. About 90 000 rotational and ro-vibrational transition frequencies have been computed on the basis of the spectroscopic constants obtained from the global fit in order to support data interpretation and astronomical searches in the interstellar medium and planetary atmospheres. Part of these data is included in the 2020 release of the HITRAN database.

Keywords: Cyanoacetylene, Interstellar matter, Molecular spectroscopy, Spectroscopic database, Energy levels, Ro-vibrational spectra

1. Introduction

Cyanoacetylene (HC_3N) is a simple linear molecule of great astrochemical interest. Its relevance has been demonstrated by the huge amount of observational studies carried out in the past decades, which revealed HC_3N to be an ubiquitous interstellar species, detected in molecular clouds [1], comets [2], nearby galaxies [3], and planetary atmospheres [4]. Recent observations have pointed out its importance as tracer

of the chemical evolution of molecular clouds [5] or — through the DC_3N isotopologue — as proxy of the deuteration level prior to the formation of dense gas in star-forming regions [6]. Moreover, cyanoacetylene emission has been used to unravel the seasonal changes and atmospheric dynamics of the largest Saturn's moon Titan [7] and is predicted to be detectable in Super-Earth atmospheres by upcoming James Webb Telescope observations [8]. Interestingly, vibrationally excited HC_3N has been also observed in Space. For example, pure rotational transitions in vibrational states up to $1100\,cm^{-1}$ have been detected in the proto-planetary nebula CRL 618 [9] (see also a more recent account for NGC 1068 [10]).

The laboratory investigation of the rotational and ro-vibrational spectra of HC_3N, which is essential for guiding astronomical searches of this species, has been pushed forward for 70 years. To date, the most comprehensive spectroscopic analysis of cyanoacetylene has been reported in our previous study (Ref. [11], hereafter Paper I), where a comprehensive list of references for laboratory detections and observations in Space is also provided. In Paper I, the HC_3N infrared spectrum has been recorded between 450 and $1100\,cm^{-1}$ and analyzed focusing on all the vibrational states with energy below $1000\,cm^{-1}$, for which a sizable number of rotational transitions were also observed. The global analysis performed in Paper I allowed to derive a consistent set of spectroscopic rotational and vibrational parameters for all the twelve vibrational states investigated, and includes the accurate modelling of two networks of anharmonic resonances which substantially perturb the spectra. Yet, the dataset of Paper I did not include any ro-vibrational transitions located in the far-infrared (FIR, here below $450\,cm^{-1}$) portion of the spectrum as well as none of the stretching bands, observed roughly between 2000 and $3400\,cm^{-1}$. While no spectrum was reported in the literature for the FIR region, some data were available for the stretching modes. In particular, after the first medium resolution (0.025–$0.050\,cm^{-1}$) study of the 1800-$6500\,cm^{-1}$ region [12], higher-resolution spectra of the ν_1 [13], ν_2 [14], ν_3 [15], and some of their hot-bands [13, 16] were reported.

Theoretical calculations involving fundamental, combination, overtone, and hot bands between 200 and $4800\,cm^{-1}$ have been recently published [17], as well as estimates for the infrared fundamental intensities [18]. Previously, various theoretical works on the force field, dipole functions, and molecular structure were also presented [19, 20, 21, 22].

However, the data available in the literature for the stretching modes indicated that the experimental dataset could be extended and recorded at a higher, homogeneous resolution. Therefore, we recently re-investigated the ν_1, ν_2, and ν_3 bands and their associated hot bands $\nu_1 + \nu_7 - \nu_7$, $\nu_2 + \nu_7 - \nu_7$, $\nu_3 + \nu_7 - \nu_7$ by Fourier transform infrared (FTIR) spectroscopy [23] at an instrumental resolution of $0.004\,cm^{-1}$.

Here, to fill the lack of HC_3N data in the FIR window, we undertake for the first time a detailed analysis of the region below $450\,cm^{-1}$, by recording FTIR spectra at the SOLEIL synchrotron facility as recently done for DC_3N [24]. In addition, a new network of anharmonic resonances involving vibrational states with energies around $1200\,cm^{-1}$ is identified and modelled on the basis of (i) spectra recorded but not analyzed in Paper I and (ii) new rotational measurements performed in this work. The ultimate goal of the present paper is to achieve an improved fit of all the HC_3N data in order to attain a very accurate and extended set of ro-vibrational constants and, consequently, a comprehensive line list to be used for astronomical observations of cyanoacetylene at different wavelengths.

2. Experiments

The new rotational and ro-vibrational spectra described in this work have been recorded in three labora-tories: the FIR spectrum has been observed at the SOLEIL synchrotron facility, while the millimeter (mm) and submillimeter (submm) spectra have been measured in Bologna and in Garching. The preparation of the sample used for the measurements has been described in Paper I.

The FIR spectrum of HC_3N has been recorded at the AILES beamline of SOLEIL using a Bruker IFS 125 FT interferometer [25] associated to a White-type multi-pass absorption cell whose optics were adjusted to obtain 150 m optical path length [26, 27]. The synchrotron radiation extracted by the AILES beamline was used as the FIR source of continuum for the FT interferometer. The interferometer was equipped with a $6\,\mu m$ Mylar-composite beamsplitter and a $4\,K$ cooled Si-bolometer and was isolated from the interferometer by two $50\,\mu m$-thick polypropylene windows. The optics compartment was continuously evacuated to $0.01\,Pa$

in order to limit the absorption of atmospheric water. Vapor of HC_3N was injected into the absorption cell at 1.5, 3.5 and 28.6 Pa pressure. The spectrum covers the range 70–500 cm^{-1} and was recorded at different pressures and with a different number of scans: 400 scans at 1.5 and 28.6 Pa, 360 scans at 1.5 Pa. The instrumental resolution was 0.001 cm^{-1}. No apodization function was applied to the interferogram. The wavenumber-axis of the spectra has been calibrated using residual water absorption lines, whose reference wavenumbers were taken from [28] and [29]. Based on the dispersion after calibration, line frequencies are expected to be as accurate as 0.0001 cm^{-1}.

A number of new mm-wave spectra have been recorded at the Center for Astrochemical Studies in the 80–175 GHz frequency interval using the CASAC spectrometer already described in details elsewhere [30]. Additional measurements in selected frequency intervals between 260 and 450 GHz have been performed in Bologna using a frequency-modulation (FM) mm-wave spectrometer, whose description has been reported in Refs. [31, 32]. In both these latter laboratories, the spectra were recorded at room temperature, using static samples at a pressure of 0.3–1.0 Pa. The transition frequencies were recovered from a line-shape analysis of the spectral profile [33] and their accuracy, estimated by repeated measurements and depending on the attained S/N, is in the 5–30 kHz range.

This work also reports on the analysis of some vibrational bands observed in the spectra previously recorded in Bologna using a Bomem DA3.002 Fourier-transform spectrometer [11, 23] and not included in Paper I. For further details about the recording conditions, the readers are referred to Bizzocchi et al. [11] and Jiang et al. [23] for the regions 450–1050 cm^{-1} and 1900–3400 cm^{-1}, respectively.

3. Observed spectra

Cyanoacetylene is a linear molecule with seven vibrational normal modes: four stretching modes (ν_1, ν_2, ν_3, ν_4; Σ symmetry) and three doubly degenerate bending modes (ν_5, ν_6, ν_7; Π symmetry). All of them are infrared active.

A portion of the vibrational energy manifold of HC_3N is schematically shown in Figure 1. All the levels involved in the present analysis are plotted in solid black lines, while the appearance of the infrared spectra is depicted sideways on the left. Our study includes all the vibrational fundamentals as well as all the excited levels below 1300 cm^{-1} with the only exception of the $v_5 = v_6 = 1$ state. This combination mode, together with the $v_5 = 2$ overtone state, is involved in a complex network of anharmonic resonances and will be the object of a future investigation. In total, 24 bands have been identified and analysed in this work. They are summarised in Table 1.

3.1. The 190–450 cm^{-1} region

The far infrared region shows many bands starting from 200 cm^{-1}. A recording of this spectral range is shown in Figure 2, together with a stick-spectrum simulation to allow for the identification of the most prominent features. The fundamental ν_7, around 220 cm^{-1}, has been observed for the first time in this work, although a precise determination of its vibrational energy had been already achieved indirectly in Paper I. Nevertheless, the resolution and sensitivity of the FIR spectrum recorded at the SOLEIL facility has confirmed and improved both precision and accuracy of the spectroscopic constants related to the ν_7 vibrational mode.

The excitation of the v_7 mode gives rise to different manifolds for increasing values of the vibrational angular quantum number l, labelled as Σ, Π, Δ, Φ, Γ, H for $l = 0, 1, 2, 3, 4, 5$, respectively. All the possible allowed transitions between those energy levels, according to the selection rule $\Delta l = \pm 1$, have been identified, with the exception of the $5\nu_7 - 4\nu_7$ hot-band, for which only the H$\leftarrow \Gamma$ component has been assigned. In the same portion of the spectrum, almost all the sub-bands of the $\nu_6 + \nu_7 - \nu_6$, $\nu_5 + \nu_7 - \nu_5$, and $\nu_6 + 2\nu_7 - \nu_6 - \nu_7$ have been also assigned, which show very weak, if not barely detectable, Q-branches.

At higher wavenumbers, the $\nu_6 - \nu_7$ (~ 277 cm^{-1}) and $\nu_4 - \nu_6$ (~ 363 cm^{-1}) difference bands, and the $2\nu_7$ overtone (~ 443 cm^{-1}) do have notable intensity as well. For all these transitions, eight associated hot bands have been identified and analysed. Apart from $\nu_4 - \nu_6$ and its $\nu_4 + \nu_7 - \nu_6 - \nu_7$ hot band, which have a prominent Q-branch ($\Delta l = \pm 1$), all these features show a parallel structure with strong P- and $R-$ branches and no Q-branch.
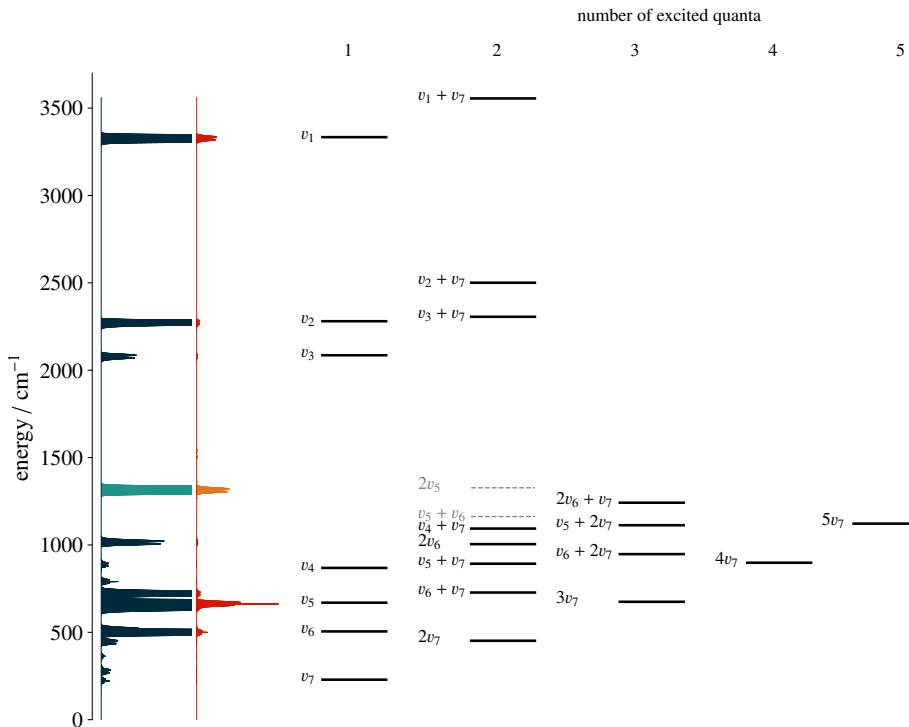
3

Figure 1: Schematic representation of the vibrational energy manifold of HC$_3$N (complete below 1300 cm^{-1}). The states investigated in this work are drawn in black solid lines. Grey dashed lines indicate the levels not considered in the present analysis. On the left, the appearance of the vibrational spectrum of HC$_3$N is depicted sideways adopting two different normalisation factors. The intensity of the red trace is adjusted to show the prominent ν_1, ν_5, and ν_6 bands, whereas the dark blue spectrum is expanded 50 times in order to show the weaker bands. Note that the $2\nu_5$ overtone (labelled with paler colour in the plots) is the only major spectral feature not covered by the present analysis (see text).

3.2. The 450–1050 cm^{-1} region

This spectral window, dominated by the very strong ν_5 fundamental and the strong ν_6 and $\nu_6 + \nu_7$ bands, has been discussed in detail in Paper I. However, some new features have been identified and analysed in this work. They are the ν_7-associated hot-bands of the ν_4 and $2\nu_6$ bands, the ν_6-associated hot-band of the $\nu_6 + \nu_7$ combination, the $2\nu_7$-associated hot-band of the ν_5 vibration, plus the new $\nu_4 + \nu_7 - \nu_6$ difference band.

3.3. The 1900–3400 cm^{-1} region

As summarized in the introduction, this region had been studied in the past by several authors, who employed different spectroscopic techniques, such as tunable diode lasers and FTIR. The re-investigation of this region was motivated by the need to have a complete coverage at a homogeneous high-resolution of the three higher energy stretching bands ν_1 (~ 3327 cm^{-1}), ν_2 (~ 2274 cm^{-1}), and ν_3 (~ 2079 cm^{-1}) and of their strongest associated hot bands. The analysis of these bands has been reported in a recent paper focused on DC$_3$N [23].

The fundamentals ν_1, ν_2, and ν_3 are all intense bands of $\Sigma - \Sigma$ symmetry, for which many P and R transitions could be assigned, up to $J = 110$ for ν_1, $J = 105$ for ν_2, and $J = 110$ for ν_3. The identification of the first hot bands $\nu_1 + \nu_7(\Pi) - \nu_7(\Pi)$, $\nu_2 + \nu_7(\Pi) - \nu_7(\Pi)$, $\nu_3 + \nu_7(\Pi) - \nu_7(\Pi)$ was rather straightforward

Table 1: Ro-vibrational bands of HC$_3$N recorded and analysed in this work.

Band	Sub-bands	Freq. range (cm^{-1})	J max	No. of lines	rms[a]$\times 10^4$ (cm^{-1})
ν_7	$\Pi - \Sigma^+$	194 - 257	106	304	0.4 (0.5)
$2\nu_7 - \nu_7$	$(\Sigma^+, \Delta) - \Pi$	196 - 253	99	654	0.6 (0.5)
$3\nu_7 - 2\nu_7$	$(\Pi, \Phi) - (\Sigma^+, \Delta)$	197 - 251	88	869	0.8 (0.75)
$4\nu_7 - 3\nu_7$	$(\Sigma^+, \Delta, \Gamma) - (\Pi, \Phi)$	199 - 249	86	858	1.2 (1.0)
$5\nu_7 - 4\nu_7$	H - Γ	209 - 240	51	115	1.3 (1.5)
$\nu_6 + \nu_7 - \nu_6$	$(\Sigma, \Delta) - \Pi$	201 - 247	81	479	1.3 (1.0)
$\nu_5 + \nu_7 - \nu_5$	$(\Sigma, \Delta) - \Pi$	202 - 248	76	405	1.2 (1.0)
$\nu_6 + 2\nu_7 - \nu_6 - \nu_7$	$(\Pi, \Phi) - (\Sigma^+, \Delta)$	205 - 247	71	266	0.2 (0.5)
$\nu_6 - \nu_7$	$\Pi - \Pi$	247 - 303	90	345	0.6 (0.75)
$\nu_6 + \nu_7 - 2\nu_7$	$(\Sigma^+, \Delta) - (\Sigma^+, \Delta)$	249 - 302	86	472	0.5 (0.75)
$2\nu_6 - \nu_6 - \nu_7$	$(\Sigma^+, \Delta) - (\Sigma^+, \Delta)$	248 - 316	89	439	1.0 (1.0)
$\nu_6 + 2\nu_7 - 3\nu_7$	$(\Pi, \Phi) - (\Pi, \Phi)$	247 - 303	91	837	1.4 (1.5)
$\nu_4 - \nu_6$	$\Sigma^+ - \Pi$	331 - 387	94	256	0.5 (0.5)
$\nu_4 + \nu_7 - \nu_6 - \nu_7$	$\Pi - (\Sigma, \Delta)$	342 - 385	72	564	1.0 (1.0)
$2\nu_7$	$\Sigma^+ - \Sigma^+$	422 - 468	88	152	0.8 (0.75)
$3\nu_7 - \nu_7$	$(\Pi, \Phi) - \Pi$	420 - 467	87	297	1.0 (1.0)
$4\nu_7 - 2\nu_7$	$(\Sigma^+, \Delta) - \Sigma^+, \Delta$	420 - 443	83	420	1.2 (1.0)
$5\nu_7 - 3\nu_7$	$(\Pi, \Phi) - (\Pi, \Phi)$	419 - 462	77	379	1.7 (1.5)
$\nu_6 + 2\nu_7 - \nu_6$	$\Pi - \Pi$	426 - 467	68	180	2.0 (2.0)
$\nu_4 + \nu_7 - \nu_6$	$\Pi - \Pi$	566 - 610	73	267	2.0 (5.0)
$\nu_5 + 2\nu_7 - 2\nu_7$	$(\Pi, \Phi) - (\Sigma^+, \Delta)$	634 - 690	105	704	2.7 (4.0)
$2\nu_6 + \nu_7 - \nu_6$	$\Pi - \Pi$	702 - 756	81	346	5.5 (5.0)
$\nu_4 + \nu_7 - \nu_7$	$\Pi - \Pi$	847 - 881	55	87	8.8 (10)
$2\nu_6 + \nu_7 - \nu_7$	$\Pi - \Pi$	991 - 1039	79	227	6.6 (5.0)

[a] Root mean square deviation of the global fit. The assumed experimental precision of each band is given in parentheses (see § 4.1).

Table 2: Rotational transitions of HC$_3$N recorded in this work.

State	Freq. range (GHz)	J max	No. of lines	rms[a] (kHz)
$v_4 = v_7 = 1$	$73 - 791$	86	83	0.209
$v_6 = 2, v_7 = 1$	$82 - 422$	45	157	0.048
$v_5 = 1, v_7 = 2$	$82 - 422$	45	155	0.043
$v_7 = 5$	$83 - 508$	54	128	0.022
inter-state	$376 - 424$	45	10	0.038

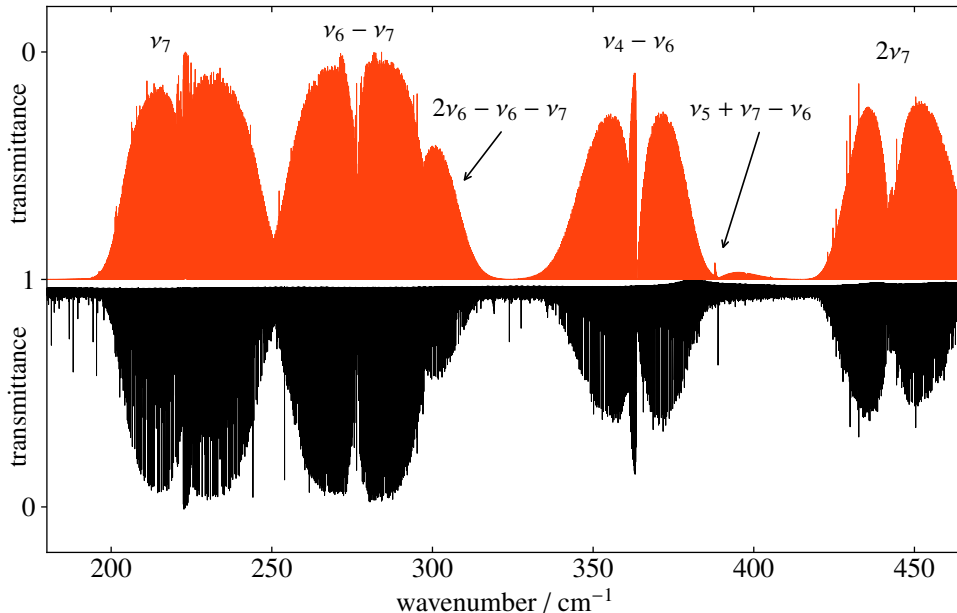[a] Root mean square deviation of the global fit.

Figure 2: Recorded FIR spectrum from 180 to 465 cm^{-1} (black trace). Synthetic transmission spectrum (orange trace) was computed based on the line list presented in this work using HITRAN Application Programming Interface (HAPI) [34]. The simulated spectrum has been displayed as reversed transmittance for a better comparison with the experimental one. Lines belonging to H$_2$O were removed from the experimental spectrum. Experimental conditions: $T = 298$ K, $P = 28.6$ Pa, $L = 150$ m, 400 scans, unapodized resolution 0.001 cm^{-1}.

and also for these bands many transitions could be assigned. The Q branches of the hot bands, although allowed by symmetry, were not detected. No evidence of strong perturbations has been found.

3.4. Rotational spectrum

The rotational spectrum of HC$_3$N has already been studied extensively in the ground and in many vibrationally excited states (see Paper I and references therein). In the context of the present investigation, we have recorded additional mm- and submm-wave data for a subset of vibrational states located between 1050 and 1200 cm^{-1}: they are $v_4 = v_7 = 1$, $(v_6 = 2, v_7 = 1)$, $(v_5 = 1, v_7 = 2)$, and $v_7 = 5$. The new measurements have been performed in Bologna and Garching focusing on selected frequency windows in the 80–450 GHz interval (an example is given in Fig. 3). A particular attention has been devoted to the $J = 40 - 46$ region (340–420 GHz) where the lines belonging to the nearly-degenerate $(v_5 = 1, v_7 = 2)$ and $v_7 = 5$ vibrational states show large deviations from their unperturbed positions owing to the avoided crossings between the various interacting sub-levels.

4. Analysis and Results

The computation of the ro-vibrational energy terms of HC$_3$N follows the procedure described in detail in Paper I. Briefly, the effective Hamiltonian is a sum of a ro-vibrational ($\tilde{H}_{\mathrm{rv}}$) and a l-type interaction ($\tilde{H}_{l\text{-type}}$) contributions, plus a term ($\tilde{H}_{\mathrm{res}}$) describing the accidental anharmonic resonances present in this molecule:

$$\tilde{H} = \tilde{H}_{\mathrm{rv}} + \tilde{H}_{l\text{-type}} + \tilde{H}_{\mathrm{res}} . \tag{1}$$
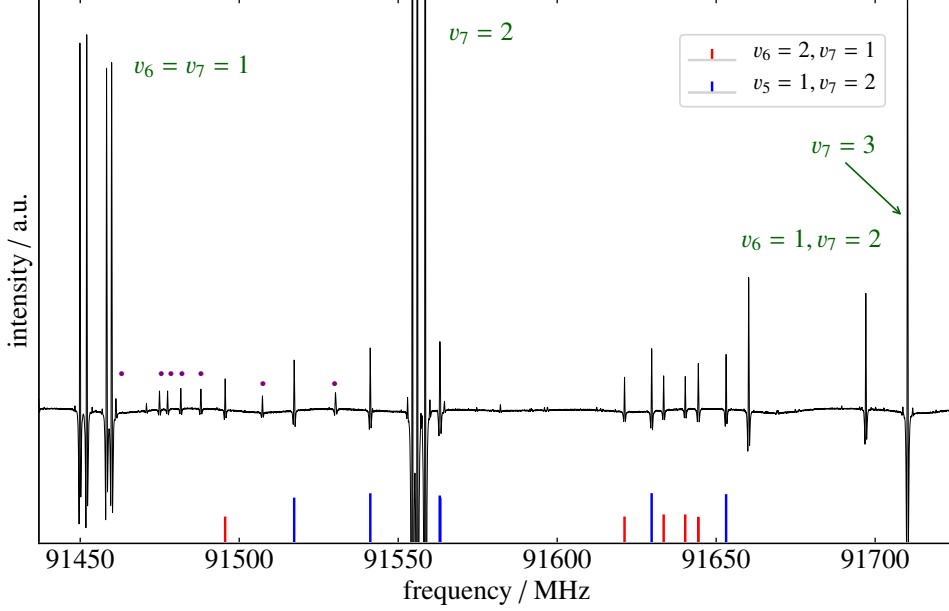
Figure 3: Excerpt of the $J = 10 \leftarrow 9$ transition of HC_3N in the region of multiple excited bending states. The stick spectrum indicates the position of the $(v_6 = 2, v_7 = 1)$ state (*red*) and $(v_5 = 1, v_7 = 2)$ (*blue*) combinations located at 1100-1200 cm^{-1}. The green labels identify the strong components belonging to some lower-energy vibrationally excited states. The purple dots mark the lines of the $(v_5 = v_6 = v_7 = 1)$ three-bending combination states which have not been analysed in this study. Spectrum recorded with the CASAC spectrometer [30] using a scan speed of $1.2\,MHz\,s^{-1}$ and $RC = 3\,ms$.

$\tilde{H}_{\mathrm{rv}}$ is diagonal in all quantum numbers, whereas $\tilde{H}_{l\text{-type}}$ gives rise to several matrix elements off-diagonal in the l_t quantum numbers and according to the selection rules $\Delta k = 0, \pm 2, \pm 4$. $\tilde{H}_{\mathrm{res}}$ contains terms connecting the sub-blocks of the nearly-degenerate, interacting vibrational states. The complete expressions of the Hamiltonian is given in Paper I.

Below 1050 cm^{-1} two networks of anharmonic interactions have been identified: (*i*) $v_5 = 1 \sim v_7 = 3$ around 660 cm^{-1} and (*ii*) $v_4 = 1 \sim v_5 = v_7 = 1 \sim v_6 = 2 \sim v_7 = 4$ centered at 880 cm^{-1}. Both resonance systems have been investigated and the corresponding interaction parameters determined from the global analysis. They are associated to the resonance Hamiltonian terms H_{30}, H_{32}, H_{40}, H_{42}, H_{50}, and H_{52}. Here, the Hamiltonian is labelled as $\tilde{H}_{mn}$, where m and n are the total degree of the vibrational and rotational operators, respectively. The same types of interaction take place if one quantum of vibrational energy is added to each energy level involved in the interactions. If the pair (*i*) is upscaled by adding one v_7 quantum, we obtain some terms of the resonance system (*ii*), whereas the same operation on (*ii*) generates a new network of interacting states located approximately at 1100 cm^{-1}: $v_4 = v_7 = 1 \sim (v_5 = 1, v_7 = 2) \sim (v_6 = 2, v_7 = 1) \sim v_7 = 5$. This resonance system has been investigated thoroughly for the first time in this work. In addition to the $\tilde{H}_{\mathrm{res}}$ terms cited above, for this analysis **we considered further contributions** produced by the $\tilde{H}_{32}$ transformed Hamiltonian:

$$\left\langle v_4, v_5^{l_5}, v_6^{l_6}, v_7^{l_7}; J, k \right| \tilde{H}_{32} \left| v_4 + 1, (v_5 - 1)^{l_5 \pm 1}, v_6^{l_6}, (v_7 - 1)^{l_7 \pm 1}; J, k \pm 2 \right\rangle$$

$$= \frac{\sqrt{2}}{2} C_{32} \left[(v_4 + 1)(v_5 \pm l_5)(v_7 \pm l_7) \right]^{1/2} \sqrt{f_{\pm 2}(J, k)}, \quad (2)$$

where the k-dependent term of the matrix element is given by (see Eq. (3b) of Paper I for the general

7

formula):

$$f_{\pm 2}(J, k) = [J(J+1) - k(k \pm 1)] [J(J+1) - (k \pm 1)(k \pm 2)] . \tag{3}$$

This interaction has been considered in association with the classic cubic anharmonic resonance $\tilde{H}_{30}$ involving the $(v_4 = v_7 = 1)$ and $(v_5 = 1, v_7 = 2)$ states and provides additional $\Delta k \pm 2$ couplings.

The ro-vibrational basis functions are chosen as product of one-/two-dimensional harmonic oscillator wave-functions and a rotational symmetric-top wave-function, $\left| v_s, v_5^{l_5}, v_6^{l_6}, v_7^{l_7}; J, k \right\rangle$, with $k = l_5 + l_6 + l_7$. In this notation v_s summarizes the stretching mode vibrational quantum numbers v_1, v_2, v_3 and v_4. Symmetry-adapted basis functions are then obtained by the Wang-type linear combinations [35]:

$$\left| v_s, v_5^{l_5}, v_6^{l_6}, v_7^{l_7}; J, k \right\rangle_{e/f}$$
$$= \frac{1}{\sqrt{2}} \left\{ \left| v_s, v_5^{l_5}, v_6^{l_6}, v_7^{l_7}; J, k \right\rangle \pm (-1)^k \left| v_s, v_5^{-l_5}, v_6^{-l_6}, v_7^{-l_7}; J, -k \right\rangle \right\} , \tag{4a}$$

$$\left| v_s, 0^0, 0^0, 0^0; J, 0 \right\rangle_e = \left| v_s, 0^0, 0^0, 0^0; J, 0 \right\rangle . \tag{4b}$$

The upper and lower signs ($\pm$) correspond to e and f wave-functions [36], respectively. For Σ states ($k = 0$), the first non-zero l_t is chosen positive.

4.1. Global fit

The analysis of the extended ro-vibrational data set has been performed following the same procedure described in details in Paper I. A total number of 533 rotational transitions and approximately 11 000 infrared lines have been added to the existing collection which now comprises a total number of 17 096 data. As usual, different weighting factors, $w = 1/\sigma^2$, have been used to take into account the unequal measurement precision (σ) of the various sources of data. The σ values for the new infrared data measured in this work are reported in the rightmost column of Table 1. For pure rotational lines, we retained the original weights of the literature data and used $\sigma = 15$ kHz for the newly measured transitions. The new data collected in the present work are summarised in Table 2.

The iterative fit procedure yields effective spectroscopic constants for each individual state, plus a set of interaction coefficients describing the accidental anharmonic resonances between nearly-degenerate vibrational states. Compared to our previous global fit, we determined the vibrational energy and the spectroscopic parameters for 4 new vibrational states, namely $v_4 = v_7 = 1$, $(v_6 = 2, v_7 = 1)$, $(v_5 = 1, v_7 = 2)$, and v_5, plus 10 more resonance coefficients. In addition, the states v_1, v_2, v_3, $v_1 = v_7 = 1$, $v_3 = v_7 = 1$, $v_3 = v_7 = 1$, already studied in Ref. [23] have been included in the present global analysis. For the constants which could not be directly determined from the fit procedure, we adopted suitable constraints. These have been derived from other states belonging to the same manifold assuming, whenever feasible, a linear v-dependence. This approach is implemented into the fitting code as described in Paper I and the whole procedure was repeated until the convergence of such derived values was achieved .

As briefly introduced in § 4, in HC$_3$N each level of the v_4 manifold is the pivot of the polyad of interacting states: $v_4 \sim (v_4 - 1, v_6 + 2) \sim (v_4 - 1, v_5 + 1, v_7 + 1) \sim (v_4 - 1, v_5 + 4)$. The fundamental polyad centered at ~ 880 cm^{-1} has been discussed in Paper I; in the following, we refer to it as the first resonance system (I RS). In this paper we investigated the polyad located at ~ 1100 cm^{-1} which includes the states $v_4 = v_7 = 1$, $(v_6 = 2, v_7 = 1)$, $(v_5 = 1, v_7 = 2)$, and $v_7 = 5$ (second resonance system, II RS, hereafter). In such a coupling scheme, a cubic interaction takes place between the $v_4 = v_7 = 1$ Π states and the Π sublevels of the $(v_6 = 2, v_7 = 1)$ and $(v_5 = 1, v_7 = 2)$ bend–bend combination; also a weak quintic **interaction** exists between $v_4 = v_7 = 1$ and $v_7 = 5$ states ($\Pi - \Pi$). In addition, the $(v_5 = 1, v_7 = 2)$ and $v_7 = 5$ states are coupled by a quartic resonance which produces effects on all their Π, Φ sublevels. The detailed scheme of the energy-level manifolds involved in this resonance system is depicted in Figure 4.

A remarkable feature of the II RS is the close vicinity of the $(v_5 = 1, v_7 = 2)$, and $v_7 = 5$ states which are coupled by the $\tilde{H}_{40}$ Hamiltonian term. The resulting perturbations **affect** both Π and Φ sub-levels, and the
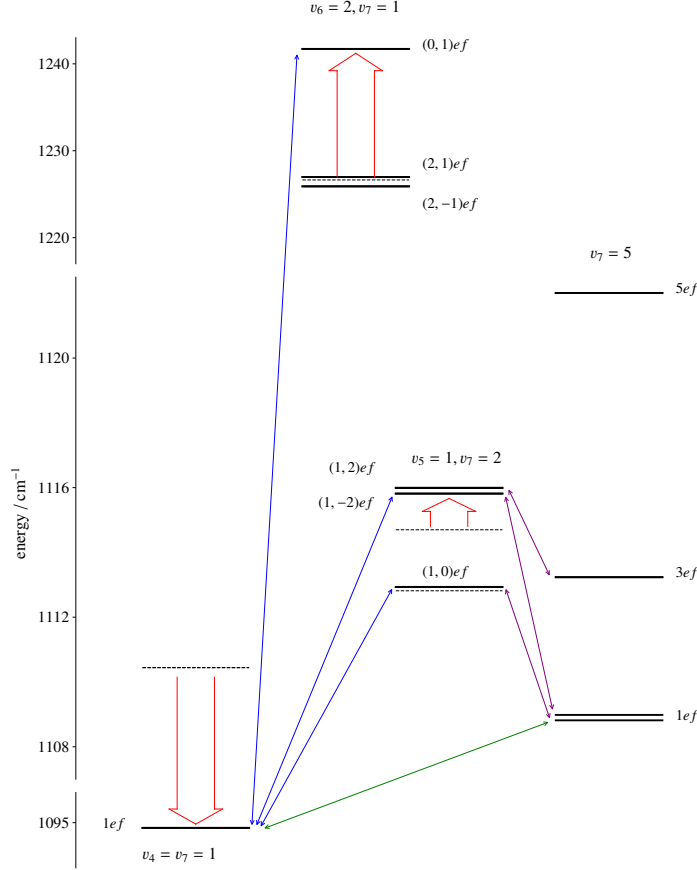
Figure 4: Vibrational energy diagram for the interacting states $v_4 = v_7 = 1$, $(v_6 = 2, v_7 = 1)$, $(v_5 = 1, v_7 = 2)$, and $v_7 = 5$ of HC$_3$N. Thin arrows indicate the main vibrational couplings relative to $\Delta k = 0$ taken into account: blue, green, and purple colors are associated to cubic ($\tilde{H}_{30}$), quartic ($\tilde{H}_{40}$), and quintic ($\tilde{H}_{50}$) interactions, respectively. Large arrows (red) illustrate the vibrational energy displacements produced by the anharmonic resonances; the unperturbed level positions are plotted with dashed lines. The weak $\Delta k = \pm 2$ interactions produced by the $\tilde{H}_{32}$ and $\tilde{H}_{42}$ Hamiltonian terms are not indicated.

corresponding lines show increasing differences from their unperturbed positions, as J approaches the value at which a given pair of interacting sublevels comes close to an exact degeneration. This is well illustrated in Figure 5 that plots the rotational energy trends for all the $(v_5 = 1, v_7 = 2)$ and $v_7 = 5$ level manifolds. The region around $J = 40$ has been extensively sampled in this work. Here the $(1, -2)^{ef}$ and $(1, 2)^{ef}$ levels of the $(v_5 = 1, v_7 = 2)$ state (here defined by the l_5 and l_7 quantum numbers only) become nearly-degenerate with the $l_7 = 3^{ef}$ levels of the $v_7 = 5$ manifold. Due to the avoided crossings, displacements up to $\sim 4\,\text{GHz}$ have been measured for some highly-perturbed lines and 10 transitions, formally labelled as "inter-state", could also be observed. A very localised anomaly is also present at $J = 12$ in the manifold of the $(v_5 = 1, v_7 = 2)$ combination. Here the $(1, 2)^e$ and the $(1, -2)^e$ sublevels, which are almost exactly degenerate, are heavily mixed because of the $\Delta k = \pm 2$ l-type resonance. As a result, two additional *intra-state* cross-over lines are generated, having half the relative intensity of the unperturbed ones. It should be underlined that, when
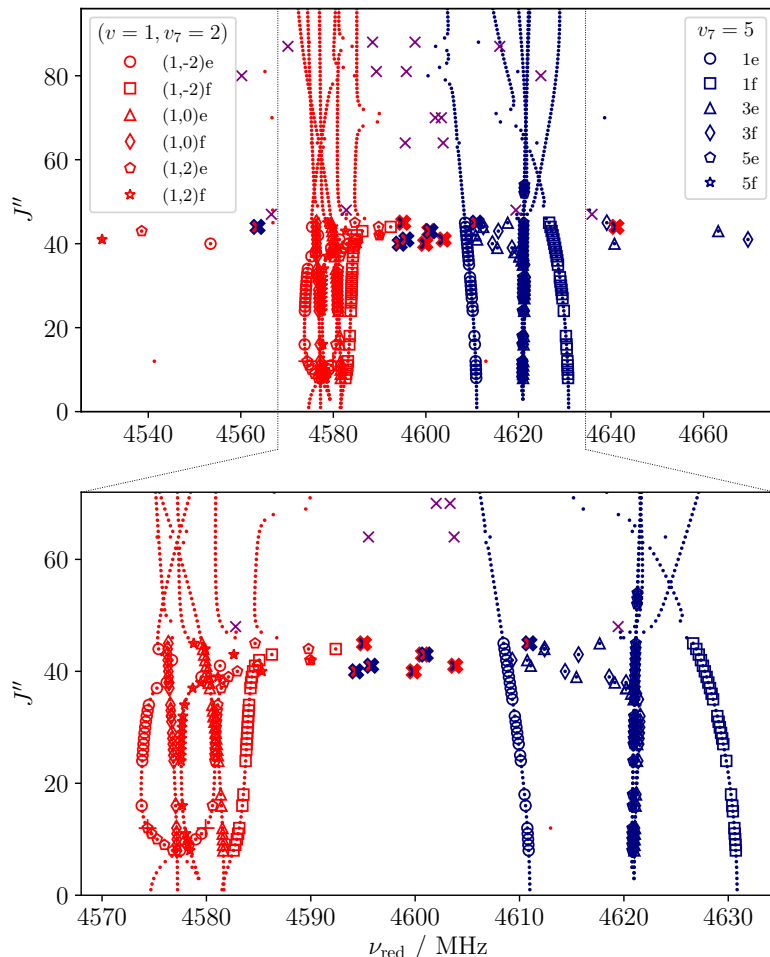
9

Figure 5: Reduced frequency diagram for the $(v_5 = 1, v_7 = 2)$, (red symbols) and $v_7 = 5$ (blue symbols) interacting states of HC$_3$N. The quantity plotted on the x-axis is $\nu_{\text{red}} = [\nu + 4D_0(J'' + 1)^3]/2(J'' + 1)$, where $D_0 = -0.5443\,\text{kHz}$ (ground-state value). Open symbols denote experimental values, whereas small dots indicate calculated values based on the parameters of Tables 3-8. Filled crosses label measured inter-state cross-over transitions, while the purple "times" symbols ($\times$) are used for those predicted by the actual model. The "plus" signs ($+$) are used for the $(v_5 = 1, v_7 = 2)$ intra-state $(1, 2)^e/(1, -2)^e$ cross-overs occurring at $J'' = 12$. The most perturbed transitions are labelled using the method implemented in the SPFIT code [37]. The bottom panel shows a detail of the upper plot in the ν_{red} range from 4568 to 4634 MHz.

a strong mixing between blocks of ro-vibrational wave-functions occurs, the labelling of the corresponding transitions become ambiguous. Our analysis tool, which uses SPFIT as the core computation routine, follows the method described by Pickett in Ref. [37].

As was the case for the I RS, we were able to completely analyse the II RS without any assumption on the energy position of the interacting levels. The network of resonances has been modelled with the same terms adopted for the I RS, the only addition being the C_{32} parameters which connects the $v_4 = v_7 = 1$ and $(v_5 = 1, v_7 = 2)$ sublevels with $\Delta k = \pm 2$. The final fit returned a weighted root-mean-square (rms)

of $\sigma_{\mathrm{w}} = 1.098$ thus indicating that, on average, the totality of the analysed data have been reproduced
within the estimated experimental uncertainties. The complete list of the fitted transitions and their *obs-calc* residuals has been deposited as supplementary material. The optimised spectroscopic constants and
resonance parameters are reported in Table 3–8.

Table 3: Spectroscopic constants derived for HC_3N in the ground and Σ^+ excited states.

Constant	Unit	Ground state	$v_4 = 1$	$v_3 = 1$	$v_2 = 1$	$v_1 = 1$
G_v	cm^{-1}		878.315(21)	2079.306095(63)	2273.994846(61)	3327.371368(61)
B_v	MHz	4549.058599(35)	4538.0994(25)	4535.1154(16)	4527.4931(15)	4541.7750(14)
D_v	kHz	0.544252(11)	0.545441(97)	0.54115(24)	0.53795(20)	0.54017(19)
H_v	mHz	0.0501(14)	0.0373(23)	0.0501[a]	0.0501[a]	0.0501[a]
L_v	nHz	$-0.299(49)$	-0.299[a]	-0.299[a]	-0.299[a]	-0.299[a]

Numbers in parentheses are one standard deviation in units of the last quoted digit.
[a] Kept fixed to ground state value.

Table 4: Spectroscopic constants derived for HC_3N in Π singly-excited bending states.

Constant	Unit	$v_7 = 1$	$v_6 = 1$	$v_5 = 1$
G_v	cm^{-1}	221.8376749(38)	498.7318990(52)	663.3685022(99)
$x_{L(tt)}$	GHz	21.823719768	6.64[a]	...
$y_{L(tt)}$	MHz	-1.9539208	...	...
B_v	MHz	4563.525607(54)	4558.301833(61)	4550.62389(12)
D_v	kHz	0.568213(10)	0.554432(11)	0.545816(19)
H_v	mHz	0.10844(55)	0.06383(61)	0.04891(95)
L_v	nHz	-0.299[b]	-0.299[b]	-0.299[b]
$d_{JL(tt)}$	kHz	-12.3148[a]	12.3200[a]	...
$h_{JL(tt)}$	Hz	0.03606[a]	...	...
$l_{JL(tt)}$	μHz	-4.33[a]	...	...
q_t	MHz	6.5386416(69)	3.5821933(50)	2.53861(11)
q_{tJ}	Hz	$-16.2807(47)$	$-2.0650(21)$	$-1.3352(78)$
q_{tJJ}	μHz	56.55(38)	...	...

Numbers in parentheses are one standard deviation in units of the last quoted digit.
[a] Assumed value, see text.
[b] Kept fixed to ground state value.

Table 5: Spectroscopic constants derived for HC_3N in Π stretching–bending combination states.

Constant	Unit	$v_4 = v_7 = 1$	$v_3 = v_7 = 1$	$v_2 = v_7 = 1$	$v_1 = v_7 = 1$
G_v	cm^{-1}	1103.5031(41)	2298.776906(58)	2493.649777(52)	3548.408143(63)
$x_{L(tt)}$	GHz	21.8235[a]	21.8235[a]	21.8235[a]	21.8235[a]
$y_{L(tt)}$	MHz	-1.955[a]	-1.955[a]	-1.955[a]	-1.955[a]
B_v	MHz	4552.4024(81)	4549.7337(20)	4541.9904(12)	4556.2057(17)
D_v	kHz	0.57387(33)	0.56679(41)	0.56164(15)	0.55491(29)
H_v	mHz	0.287(15)	0.1092[a]	0.1092[a]	0.1092[a]
L_v	nHz	-0.299[b]	-0.299[b]	-0.299[b]	-0.299[b]
$d_{JL(tt)}$	kHz	-12.3148[a]	-12.3148[a]	-12.3148[a]	-12.3148[a]
$h_{JL(tt)}$	Hz	0.03606[a]	0.03606[a]	0.03606[a]	0.03606[a]
$l_{JL(tt)}$	μHz	-4.33[a]	-4.33[a]	-4.33[a]	-4.33[a]
q_t	MHz	6.5551(18)	6.4572(24)	6.6500(15)	6.5426(21)
q_{tJ}	Hz	$-17.293(60)$	$-14.95(61)$	$-18.27(24)$	$-17.33(46)$
q_{tJJ}	μHz	56.55[a]	56.55[a]	56.55[a]	56.55[a]

Numbers in parentheses are one standard deviation in units of the last quoted digit.
[a] Assumed value, see text.
[b] Kept fixed to ground state value.

Table 6: Spectroscopic constants derived for HC$_3$N in bending overtone states.

Constant	Unit	$v_7 = 2$	$v_7 = 3$	$v_7 = 4$	$v_7 = 5$	$v_6 = 2$
G_v	cm^{-1}	442.8985684(47)	663.2245907(88)	882.85094(25)	1101.828055(78)	997.905(20)
$x_{L(tt)}$	GHz	21.633441(35)	21.449844(33)	21.2833(19)	21.06947(24)	6.64(15)
$y_{L(tt)}$	MHz	−1.955[a]	−1.955[a]	−1.955(88)	−0.3497(62)	...
B_v	MHz	4577.967127(70)	4592.38377(12)	4606.77415(34)	4621.15002(20)	4567.4545(19)
D_v	kHz	0.5926296(98)	0.617401(24)	0.642542(19)	0.668160(46)	0.564555(16)
H_v	mHz	0.16383(50)	0.2168(13)	0.2678(10)	0.3217[a]	0.07550(90)
L_v	nHz	−0.299[b]	−0.299[b]	−0.299[b]	−0.299[b]	−0.299[b]
$d_{JL(tt)}$	kHz	−13.254(20)	−14.076(18)	−14.794(22)	−15.954(11)	12.32(48)
$h_{JL(tt)}$	Hz	0.0549(16)	0.0819(37)	0.1028(20)	0.1196(27)	...
$l_{JL(tt)}$	μHz	−3.96[a]	−3.58(20)	−3.20(11)	−2.82[a]	...
q_t	MHz	6.563420(91)	6.587570(26)	6.612141(46)	6.635470(84)	3.5821947[a]
q_{tJ}	Hz	−16.623(17)	−16.9246(86)	−17.270(11)	−17.379(28)	−2.0650[a]
q_{tJJ}	μHz	55.41(88)	54.92(57)	55.62(63)	54.81[a]	...
u_{77}	Hz	−0.11185[a]	−0.10874(37)	−0.10560(49)	−0.0720(33)	...

Numbers in parentheses are one standard deviation in units of the last quoted digit.

[a] Assumed value, see text.

[b] Kept fixed to ground state value.

13

Table 7: Spectroscopic constants derived for HC$_3$N in bending combination states.

Constant	Unit	$v_6=v_7=1$	$v_6=1, v_7=2$	$v_6=2, v_7=1$	$v_5=v_7=1$	$v_5=1, v_7=2$
G_v	cm^{-1}	720.2880301(52)	941.068193(20)	1219.179425(99)	885.37212(74)	1106.6535(14)
$x_{L(tt)}$	GHz	6.64[a]	6.64[a]	6.64[a]	...	...
$x_{L(77)}$	GHz	21.82354[a]	21.66088(22)	21.82354[a]	21.82354[a]	21.7050(11)
$y_{L(77)}$	MHz	−1.955[a]	−1.955[a]	−1.955[a]	−1.955[a]	−1.955[a]
$x_{L(t7)}$	GHz	17.12559(10)	17.12588(13)	17.1062(13)	19.248(23)	18.322(20)
r_{t7}	GHz	−11.77215(14)	−11.49987(62)	−12.2727(42)	7.058(46)	8.999(40)
r_{t7J}	kHz	−12.725(66)	−9.810(97)	−12.725	−0.0269(16)	−68.4(26)
r_{t7JJ}	Hz	1.829(80)	2.091(16)	1.829[a]	1.02(10)	1.01[a]
B_v	MHz	4572.864613(61)	4587.39084(16)	4582.11183(11)	4565.08437(95)	4579.4837(28)
D_v	kHz	0.578247(11)	0.602593(11)	0.587720(33)	0.569732(25)	0.592232(83)
H_v	mHz	0.13130(67)	0.19702(64)	0.04996[a]	0.10621(76)	0.10628[a]
L_v	nHz	−0.299[b]	−0.299[b]	−0.299[b]	−0.299[b]	−0.299[b]
$d_{JL(tt)}$	kHz	12.3200[a]	12.3200[a]	12.3200[a]	...	...
$d_{JL(77)}$	kHz	−12.3148[a]	−6.477(56)	−12.3148[a]	−12.3148[a]	−19.49(17)
$h_{JL(77)}$	Hz	0.03606[a]	0.03606[a]	0.03606[a]	0.03606[a]	0.05760[a]
$l_{JL(77)}$	μHz	−4.3349[a]	−4.3349[a]	−4.3349[a]	−4.3349[a]	−3.9556[a]
$d_{JL(t7)}$	kHz	55.652(83)	50.390(46)	55.186(68)	−20.22(72)	6.5(13)
$h_{JL(t7)}$	Hz	...	...	...	0.90(12)	0.90[a]
q_t	MHz	3.62252(40)	3.67226(27)	3.622253[a]	2.56559(26)	2.5607(13)
$q_{t.J}$	Hz	−2.2691[a]	−2.4735(94)	−2.0645[a]	−1.439(11)	−1.439[a]
q_7	MHz	6.59296(19)	6.61721(12)	6.63503(41)	6.53864[b]	6.5552(11)
$q_{7.J}$	Hz	−16.359(11)	−16.6393(67)	−16.427(99)	−16.281[b]	−16.840(71)
$q_{7.JJ}$	μHz	56.55[a]	55.41[a]	56.55[a]	56.55[b]	56.55[a]
u_{77}	Hz	...	−0.0909(28)	...	...	...
u_{t7}	Hz	−2.008(83)	−2.317(16)	−0.073(20)	−1.00(13)	−0.912(81)
q_{t77}	kHz	...	−14.846(64)	...	...	−2.218(54)

Numbers in parentheses are one standard deviation in units of the last quoted digit.

[a] Assumed value, see text.

[b] Kept fixed to ground state value.

Table 8: Resonance parameters.

Interacting states	Parameter	Unit	Value
$(v_5 = 1) - (v_7 = 3)$	C_{40}	MHz	791.17(98)
$(v_5 = 1) - (v_7 = 3)$	C_{42}^J	MHz	$-0.0253(30)$
$(v_5 = v_7 = 1) - (v_7 = 4)$	C_{40}	MHz	742.2(51)
$(v_5 = v_7 = 1) - (v_7 = 4)$	C_{42}^J	MHz	0.1339(67)
$(v_4 = 1) - (v_6 = 2)$	C_{30}	cm^{-1}	16.0313(95)
$(v_4 = 1) - (v_6 = 2)$	C_{32}^J	MHz	$-0.5164(23)$
$(v_4 = 1) - (v_5 = v_7 = 1)$	C_{30}	cm^{-1}	$-2.4109(40)$
$(v_4 = 1) - (v_7 = 4)$	C_{50}	MHz	3498(29)
$(v_4 = 1) - (v_7 = 4)$	C_{52}^J	kHz	35.4(14)
$(v_5 = v_7 = 1) - (v_7 = 4)$	C_{42a}	kHz	21.08(84)
$(v_5 = v_7 = 1) - (v_7 = 4)$	C_{42b}	kHz	8.33(51)
$(v_5 = 1, v_7 = 2) - (v_7 = 5)$	C_{40}	MHz	938.0(32)
$(v_5 = 1, v_7 = 2) - (v_7 = 5)$	C_{42}^J	MHz	$-0.0283(17)$
$(v_4 = 1, v_7 = 1) - (v_6 = 2, v_7 = 1)$	C_{30}	cm^{-1}	15.94393(30)
$(v_4 = 1, v_7 = 1) - (v_6 = 2, v_7 = 1)$	C_{32}^J	MHz	$-0.53450(52)$
$(v_4 = 1, v_7 = 1) - (v_5 = 1, v_7 = 2)$	C_{30}	cm^{-1}	$-2.2338(33)$
$(v_4 = 1, v_7 = 1) - (v_5 = 1, v_7 = 2)$	C_{32}^J	MHz	$-0.0626(65)$
$(v_4 = 1, v_7 = 1) - (v_7 = 5)$	C_{50}	MHz	2825.8(30)
$(v_5 = 1, v_7 = 2) - (v_7 = 5)$	C_{42a}	kHz	1.11(18)
$(v_5 = 1, v_7 = 2) - (v_7 = 5)$	C_{42b}	kHz	$-3.917(88)$
$(v_4 = 1, v_7 = 1) - (v_5 = 1, v_7 = 2)$	C_{32}	kHz	$-18.8(16)$

Numbers in parentheses are one standard deviation in units of the last quoted digit.

4.2. Ab initio calculations

Very accurate predictions of molecular structures as well as of spectroscopic properties can be obtained by combining calculations at the coupled-cluster (CC) level of theory, with single and double excitations augmented by a perturbative treatment of triple excitations, i.e. CCSD(T) [38], within composite schemes for incorporating both the basis-set truncation and core-correlation effects. In the present work, the equilibrium structure of HC_3N has been obtained by applying the approach based on the additivity of the most relevant terms directly to the geometrical parameters (see, for example, [39, 40, 41]). Complete basis set (CBS) extrapolations were performed for both the Hartree-Fock self-consistent-field (HF-SCF) energy and the CCSD(T) correlation energy within the frozen-core (fc) approximation, employing the formulas of Halkier et al. [42] for the former, while the two-parameter correction of Helgaker et al. [43] was used for the latter. The correlation-consistent polarised basis sets cc-pVnZ (n=Q,5,6) by Dunning et al. [44, 45] were used, with n=Q,5,6 for HF-SCF and N=Q,5 for CCSD(T). The core-valence (CV) correlation term was computed (at the CCSD(T) level of theory) as the difference between the all-electron (ae) and frozen-core data using the cc-pCVQZ basis set [45]. By combining the CBS and CV terms, the best-estimate geometry, hereafter referred to as CCSD(T)/CBS+CV, was obtained. All the calculations were carried out using the CFOUR suite of programs [46] and its implementation of analytic second derivatives [47], while the anharmonic contributions to vibrational data and spectroscopic constants were calculated within the framework of 2nd-order vibrational perturbation theory (VPT2) and using an appropriate suite of programs [48] implementing the formulas reported in the literature (see Refs. [49, 50, 51]). The cubic and quartic semi-diagonal force constants needed to obtain these corrections were calculated at the fc-CCSD(T) level of theory and using the cc-pVQZ basis set.

The comparison between a selection of ab initio computed parameters and the corresponding experimental values are reported in Table 9. They include, vibration-rotation interaction constants (α_r), l-type doubling coefficients (q and q_J), anharmonicity constants ($x_{L(tt')}$), and vibrational l-type doubling parameters ($r_{tt'}$). The agreement between experimentally derived and ab initio computed values is excellent for all the ro-vibrational parameters, except for α_4, ($\sim 5\%$), α_5, ($\sim 9\%$), q_5, ($\sim 5\%$), and q_{5J}, ($\sim 30\%$). These constants are derived from vibrational fundamentals affected by anharmonic resonances ($v_4 = 1$ and $v_5 = 1$), thus their experimental values may include spurious contributions, not completely removed by the variational treatment.

It is worthwhile to note that our best-estimate geometry is in remarkable agreement with the semi-experimental equilibrium structure determined by Botschwina [22]. Actually, the comparison between our values ($r_{HC} = 1.0624$ Å, $r_{CC} = 1.2049$ Å, $r_{CC} = 1.13776$ Å and $r_{CN} = 1.1606$ Å) and those of Ref. [22] ($r_{HC} = 1.0623$ Å, $r_{CC} = 1.2059$ Å, $r_{CC} = 1.3761$ Å and $r_{CN} = 1.1606$ Å) points out an average error around 0.7 mÅ with a maximum deviation of 1.5 mÅ.

Focusing on the vibrational anharmonicity constants, it should be noted that some of the $x_{L(tt')}$ and $r_{tt'}$ coefficients contain near-singular denominators in their VPT2 formulation when $\omega_s \approx 2\omega_t$ or $\omega_s \approx \omega_t + \omega_{t'}$ [49]. Such terms should be removed from the theoretically computed constants in order to allow for a meaningful comparison with the values derived from the spectral analysis, in which the resonances are explicitly treated, thus yielding "deperturbed" Hamiltonian coefficients. These corrected parameters have been marked with an asterisk in Table 9 and the problematic terms have been be factored out as follows:

$$x_{L(tt)} = x^*_{L(tt)} - \frac{1}{32}\phi^2_{stt}(2\omega_t - \omega_s)^{-1}, \tag{5a}$$

$$x_{L(tt')} = x^*_{L(tt')} - \frac{1}{16}\phi^2_{stt'}(\omega_t + \omega_{t'} - \omega_s)^{-1}, \tag{5b}$$

$$r_{tt'} = r^*_{tt'} + \frac{1}{8}\phi^2_{stt'}(\omega_t + \omega_{t'} - \omega_s)^{-1}. \tag{5c}$$

As it can be seen, the experimental values of these anharmonic quantities compare generally well with their ab initio counterparts, but two cases of strong disagreement are present: $x_{L(66)}$ and r_{57}. Both these parameters derive from the analysis of heavily perturbed energy level manifold, thus they retain certain degree of effectiveness. From the theoretical side, it should be noted that the magnitude of the singular

terms expressed by Eq. (5a) and (5c) is large: contributions of about 100 GHz and 21 GHz have been removed from the VPT2 computed $x_{L(66)}$ and r_{57}, respectively, to obtain the final (actually smaller) deperturbed values. As a result, the theoretical estimates of these quantities should be regarded with caution as they are very sensitive to any small numerical inaccuracy in the involved quadratic and cubic potential constants.

Table 9: Comparison between experimental and calculated *ab initio* spectroscopic constants of HC_3N.

Constant	Unit	Experimental[a]	ab initio[b]
α_1	MHz	7.2836	7.030
α_2	MHz	21.5655	21.585
α_3	MHz	13.9432	13.765
α_4	MHz	10.9592	10.445
α_5	MHz	-1.5653	-1.714
α_6	MHz	-9.2432	-9.234
α_7	MHz	-14.4670	-14.389
q_5	MHz	2.5386	2.4052
q_6	MHz	3.5822	3.508
q_7	MHz	6.5386	6.425
q_{5J}	Hz	-1.34	-0.896
q_{6J}	Hz	-2.07	-1.81
q_{7J}	Hz	-16.28	-15.04
$x_{L(55)}$	GHz	. . .	159.1
$x_{L(66)}^*$	GHz	6.64	-29.53
$x_{L(77)}$	GHz	21.823	21.52
$x_{L(56)}$	GHz	. . .	0.0
$x_{L(57)}^*$	GHz	19.248	16.24
$x_{L(67)}$	GHz	17.126	17.15
r_{56}	GHz	. . .	50.07
r_{57}^*	GHz	7.058	4.44
r_{67}	GHz	-11.772	-11.69

[a] From constants of Tables 3–8.
[b] Derived from VPT2 formulas using the force constants computed at the fc-CCSD(T) level in conjunction with cc-pV5Z (harmonic) and cc-pVQZ (cubic and quartic force field) basis set. Asterisks denote deperturbed values (see text).

5. Line list

Given the importance of HC_3N as astrochemical tracer, the set of spectroscopic constants obtained from the global fit has been used to predict an extended line list of rest frequencies which includes all observed lines, both rotational and ro-vibrational, and many other transitions of both types that could be predicted within their expected experimental uncertainty. The line list of about 90 000 transitions was calculated in the region 0–3600 cm^{-1} with 68 927 transitions from this list adapted for the HITRAN2020 database [52].

17

A coherent computation of the line relative intensities for a comprehensive data set as such described in this work requires some care. More specifically, when dealing with the various sub-bands of a transition involving multiply-excited bending states, one should consider the various numerical factors arising from the different v_t, l_t excitation and from the symmetrised form of the rovibrational basis. The issue has been already recognised in Ref. [53] and beforehand treated in some details by Fayt et al. [54]. In this latter work, however, the formulation is specifically tailored for the ν_9 band systems of NC_4N and cannot be applied directly to our HC_3N data set. The procedure adopted in this work to carry out accurate and consistent intensity calculations is reported in detail in Appendix A.

Briefly, we derived the transition moment of a single ro-vibrational line from the only experimental data available in literature, namely the integrated band intensities of Ref. [53]. As far as the pure rotational transitions are concerned, DeLeon et al. [55] reported the experimental determination of the dipole moments in the ground, $v_7=1$ and $v_6=1$ states. All dipole moments relative to rotational transitions in other excited vibrational states were either derived from the experimental ones, when feasible, or fixed to the ground state value. Such transition and dipole moments were used as input information for the SPCAT routines [37] in order to obtain a calculated value for the intensities of all the transitions included in the database we produced. The comparison with the intensity values [53] reported in HITRAN2016 database [56] shows a substantial agreement. On the contrary, there is a discrepancy with the intensity of the ν_1 fundamental band at $\sim 3\mu m$ (which was not provided in HITRAN2016) calculated in Ref. [57] to model cometary atmospheres. The values from Ref. [57] are approximately three times greater than those derived in this work. Since our calculations reproduce accurately the relative intensity of the observed infrared bands over a wide range and they match the values reported in HITRAN2016 for the FIR bands, we are confident about their reliability.

6. Conclusions

In this paper we present the most detailed and extended analysis of the rotational and high-resolution ro-vibrational spectra of HC_3N to date. All fundamental bands and a considerable number of hot and combination bands have been observed experimentally. A global fit including all transitions already published and the new set of far infrared and rotational data has been performed and a very accurate set of rotational, centrifugal distortion, vibrational, and l-doubling parameters has been obtained. Moreover, two networks of anharmonic resonances have been observed and included in the total Hamiltonian. Their analysis has allowed the determination of 21 resonance constants. A number of spectroscopic constants have been calculated from an *ab initio* anharmonic force field. Their agreement with the corresponding experimental parameters is very good.

About 90 000 rotational and ro-vibrational transition energies have been predicted on the basis of the molecular constants obtained from the global fit. This calculated database includes a large number of unobserved transitions, which however were confidently predicted within their expected average experimental uncertainty. Intensity calculations have been performed for all the lines of the database. If compared to the HITRAN2016 database, the ro-vibrational intensities show a general agreement. As far as the rotational lines are concerned, the new database HITRAN2020, which includes our line list, contains a much larger number of transitions. Also, some sets of transitions mislabelled or with a wrong intensity value have been corrected.

Although the line list in HITRAN2016 [56] includes almost 180 000 transitions, no ro-vibrational data are present below 463.6 cm^{-1} or above 759.0 cm^{-1}. Therefore, our list is more complete in terms of total spectral window, since it covers all vibrational modes. It is less complete in terms of vibrational transitions, as hot and combination bands involving highly excited vibrational states were not considered because of their negligible intensity. The HITRAN2020 edition of the database [52] now employs our line list below 463.6 cm^{-1} and above 759.0 cm^{-1}.

In conclusion, this paper provides an accurate and precise set of spectroscopic constants for HC_3N, which can be used to test high level ab initio calculations. Moreover, a reliable list of rest frequencies and intensities is presented. This database is of considerable importance when the detailed and quantitative interpretation of spectra of remote environments, such as planetary atmospheres or any other space environment is required.

Appendix A. Intensity calculation

The experimental integrated band intensities are reported in Tables 1 and 2 of Ref. [53]. A theoretical description for such quantity can be derived from the expression of an individual ro-vibrational transition $a, J' \leftarrow b, J''$ (J is the rotational quantum number and a and b summarize all other quantum numbers) of a bulk system of N molecules at temperature T.

$$I_{rv}^N(T) = \frac{\gamma_i \pi \nu_{rv} n_L T_0}{p_0 T} \frac{S_{aJ',bJ''}}{3\epsilon_0 \hbar c} \frac{e^{-E''_{rv}/kT}(1 - e^{-h\nu_{rv}/kT})}{Q_{rv}(T)}, \tag{A.1}$$

where ν_{rv} is the transition frequency, γ_i the isotopic fractional abundance, $Q_{vr}(T)$ the total rovibrational partition function at T, n_L the Loschmidt number at $p_0 = 1\,\text{atm}$ and $T_0 = 273.15\,\text{K}$, E''_{rv} is the energy of the lower state and $S_{aJ',bJ''}$ the line strength. $S_{aJ',bJ''}$ can be factored as follows:

$$S_{aJ',bJ''} = \Theta_{ab}^2 L(J', J'', k', k'') W_{ab}, \tag{A.2}$$

in which Θ_{ab} is the dipole moment derivative for the $a \leftarrow b$ vibrational transition, $L(J', J'', k', k'')$ the Hönl-London factor and W_{ab} is a numerical factor. $S_{aJ',bJ''}$ will be discussed in more detail later. By re-elaborating Eq. (A.1) we obtain

$$I_{rv}^N(T) = \frac{8\pi^3 n_L T_0}{3p_0 hc} \frac{1}{4\pi\epsilon_0} \gamma_i \nu_{rv} \Theta_{ab}^2 W_{ab} \frac{L(J', J'', k', k'') e^{-E''_r/kT}}{Q_r(T)} \frac{(1 - e^{-h\nu_{rv}/kT}) e^{-E''_v/kT}}{TQ_v(T)}. \tag{A.3}$$

In the expression above we assumed $E_{rv} = E_v + E_r$, and $Q_{rv}(T) = Q_v(T)Q_r(T)$. In order to obtain the integrated band intensity we need to sum over all possible transitions (P, Q and R) of a given band starting from any initial level defined by J''. Namely

$$I_{rv}(T) = \sum_{J''} \sum_{P,Q,R} I_{rv}^N(T). \tag{A.4}$$

Considering that

$$\sum_{P,Q,R} L(J', J'', k', k'') = 2J'' + 1, \tag{A.5a}$$

$$\sum_{J''} \frac{2J'' + 1}{Q_r(T)} e^{-E''_r/kT} = 1, \tag{A.5b}$$

equation (A.4) can be written as

$$I_{rv}(T) = \frac{8\pi^3 n_L T_0}{3p_0 hc} \frac{1}{4\pi\epsilon_0} \gamma_i \nu_0 \Theta_{ab}^2 W_{ab} \frac{(1 - e^{-h\nu_0/kT})}{TQ_v(T)}, \tag{A.6}$$

where all rotational terms have been removed. The constants in equation (A.6) are taken from CODATA 2018 [58] and are: $n_{\rm L} = 2.686780111 \times 10^{19}\,{\rm mol\,cm^{-3}}$, $T_0 = 273.15\,{\rm K}$, $p_0 = 1$ atm, $h = 6.62607015 \times 10^{-27}\,{\rm erg\,s}$, $c = 2.99792458 \times 10^{10}\,{\rm cm\,s^{-1}}$, $1/4\pi\epsilon_0 = 10^{-36}\,{\rm erg\,cm^3\,D^{-2}}$. Since Θ_{ab}^2 is measured in D^2 and ν_0 in cm^{-1}, the intensity is expressed in units of $cm^{-2}\,atm^{-1}$. Moreover, we can safely assume that $\nu_{\rm rv}$ is equal to the band origin ν_0. The purely vibrational exponential is equal to 1, as the ground state vibrational energy is set to zero. By substitution of the above constants we eventually have:

$$I_{\rm rv}(T) = 3054.74207\,\gamma_i\nu_0\Theta_{ab}^2 W_{ab}\,\frac{(1 - {\rm e}^{-h\nu_0/kT})}{TQ_{\rm v}(T)}\,. \qquad (A.7)$$

The factor 3054.74207 is the same reported in Ref. [59]. If a band system is considered, the total intensity is given by a sum over all populated vibrational states obtained by multiplying $I_{\rm rv}(T)$ by the vibrational partition function. We therefore obtain:

$$I_{\rm rv}^{BS}(T) = 3054.74207\,\gamma_i\nu_0\Theta_{ab}^2 W_{ab}\,\frac{(1 - {\rm e}^{-h\nu_0/kT})}{T}\,. \qquad (A.8)$$

$I_{\rm rv}^{BS}(T)$ is directly comparable with the integrated band intensities given in Ref. [53].

The line strength of Eq. (A.2) gives rise to rotational and vibrational factors symbolically defined as L and W_{ab}. Following the procedure of Refs. [50, 60], the line strength of an allowed rovibrational transition $(a, J' \leftarrow b, J'')$ can be expressed as

$$S_{aJ',bJ''} = \sum_{f,M',M''} |\langle aJ'M'| M_f |bJ''M''\rangle|^2\,, \qquad (A.9)$$

where a and b collect all the quantum numbers not indicated explicitly (see later), and M_f are the space-fixed components of the electric dipole moment.

The following steps are then taken:

i. the dipole moment operator is expressed in terms of the molecule-fixed components μ_γ and the rotation matrices $\mathscr{D}_{f\gamma}^{(1)}(\omega)^*$ through $M_f = \sum_\gamma \mathscr{D}_{f\gamma}^{(1)}(\omega)^*\mu_\gamma$ [61];

ii. the dipole moment components μ_γ are expanded as a function of the normal coordinates q_r:
$\mu_\gamma = \mu_{\rm e}^\gamma + \sum_r \mu_r^\gamma q_r + \sum_{r,s} \mu_{rs}^\gamma q_r q_s + \ldots = \mu_{00}^\gamma + \mu_{10}^\gamma + \mu_{20}^\gamma + \ldots$; μ_r^γ and μ_{rs}^γ are the first and second derivatives of the dipole moment with respect to the normal coordinates;

iii. if only the μ_{10}^γ and μ_{20}^γ terms are maintained, the fundamental, overtone, combination, and difference bands with $\sum_r |\Delta v_r| = 2$ are accounted for, and the M_f components become $M_f = \mathscr{D}_{f\gamma}^{(1)}(\omega)^*\mu_{10}^\gamma + \mathscr{D}_{f\gamma}^{(1)}(\omega)^*\mu_{20}^\gamma = M_{11}^f + M_{21}^f$;

iv. the ro-vibrational wave-functions are factorised as $|aJM\rangle = \sum_{l,k} a_{vlk} |v,l\rangle |J,k,M\rangle$, where v and l represent all vibrational quantum numbers and $k = \sum_t l_t$.

The line strength expression thus becomes:

$$S_{aJ',bJ''} = \sum_{f,M',M''} \left|\langle aJ'M'| M_{11}^f + M_{21}^f |bJ''M''\rangle\right|^2\,, \qquad (A.10a)$$

$$S_{aJ',bJ''} = \sum_{f,M',M''} \left|\sum_{l',l'',k',k''} a_{v'l'k'}^\star b_{v''l''k''} \langle v',l'| \mu_{10}^\gamma + \mu_{20}^\gamma |v'',l''\rangle \langle J',k',M'| \mathscr{D}_{f\gamma}^{(1)}(\omega)^* |J'',k'',M''\rangle\right|^2\,.$$
$$(A.10b)$$

By evaluating the integral over the rotation matrices, the sum over the space-fixed variables f, M', M'', and applying the sum rules for the $3j$-symbols, the intensity integral becomes [60]:

20

$$S_{aJ',bJ''} = \left| \sum_{k',k''} a^\star_{v'l'k'} b_{v''l''k''} \langle v',l'| \, \mu_{10}^{k'-k''} + \mu_{20}^{k'-k''} \, |v'',l''\rangle \right.$$

$$\left. \times [(2J'+1)(2J''+1)]^{1/2} \begin{pmatrix} J' & 1 & J'' \\ -k' & k'-k'' & k'' \end{pmatrix} \right|^2 . \qquad (A.11)$$

The sum in Eq. (A.11) can include one, two, or four terms, because it runs over degenerate states described by the symmetry-adapted basis functions defined in Eqs. (4). In this work, Eq. (A.11) has been implemented in a automatic routine that computes the vibrational intensity factors using the appropriate symmetrised basis functions.

As already mentioned, the dipole moment operators in Eq. (A.11) will apply to different vibrational transitions: M_{11}^f to the fundamental bands and M_{21}^f, to the first overtones, combinations, and difference bands. Their dependence from the vibrational coordinates can be conveniently expressed in terms of products of the ladder operators [62]. For instance, the dipole moment for fundamental vibrational transitions is:

$$\mu_{10}^\gamma = \frac{1}{2} \sum_s \Theta_s \left(\hat{\mathscr{L}}_s^+ + \hat{\mathscr{L}}_s^- \right) + \sum_t \Theta_t \left[\left(\hat{\mathscr{L}}_{t,+}^+ - \hat{\mathscr{L}}_{t,-}^+ \right) + \left(\hat{\mathscr{L}}_{t,-}^- - \hat{\mathscr{L}}_{t,+}^- \right) \right] , \qquad (A.12)$$

where Θ_r ($r = s, t$) is a coefficient proportional to the dipole moment derivatives and s and t denotes non-degenerate (stretching) and doubly-degenerate (bending) normal modes, respectively. The sums of operators above are needed to ensure that the operator is Hermitian. To give an example, the line strength of a $J' \leftarrow J''$ P or R transition of the ν_7 fundamental perpendicular band can be derived from Eq. (A.12), if we consider only the terms for $t = 7$, as

$$\mu_{10,7}^{(1)} = \Theta_7 \left(\hat{\mathscr{L}}_{7,+}^+ - \hat{\mathscr{L}}_{7,-}^+ + \hat{\mathscr{L}}_{7,-}^- - \hat{\mathscr{L}}_{7,+}^- \right) , \qquad (A.13)$$

where $\mu^{(\pm 1)} = \mu_x \pm i\mu_y$ for the spherical components of the dipole moment operator. The wavefunctions of the ro-vibrational states involved in the transition, described with a simplified notation of Eqs. (4) $|v_7, l_7\rangle$, are $|0,0\rangle$ for the ground state and $\frac{1}{\sqrt{2}} \{|1,1\rangle - |1,-1\rangle\}$ for the upper state of e parity.

By substituting Eq. (A.13) in Eq. (A.11), the non-vanishing terms give rise to the following line strength expression:

$$S_{\nu_7, J' \leftarrow J''} = \frac{(\Theta_7)^2}{2} \left| \left\{ \langle 1,1| \hat{\mathscr{L}}_{7,+}^+ |0,0\rangle \begin{pmatrix} J' & 1 & J'' \\ -1 & 1 & 0 \end{pmatrix} + \langle 1,-1| \hat{\mathscr{L}}_{7,-}^+ |0,0\rangle \begin{pmatrix} J' & 1 & J'' \\ 1 & -1 & 0 \end{pmatrix} \right\} \right|^2$$

$$\times (2J'+1)(2J''+1) = 2(\Theta_7)^2 (2J'+1)(2J''+1) \begin{pmatrix} J' & 1 & J'' \\ 1 & -1 & 0 \end{pmatrix}^2 . \qquad (A.14)$$

The term involving only rotational quantum numbers is the Hönl-London factor. It can be shown, by applying the algebraic expression of the $3j$-symbols, that Eq. (A.14) is equivalent to Eqs. (24)–(26) of Ref. [54] for the P, R branches[1].

The Θ_r, Θ_{rs} coefficients, used as input for the SPCAT routines [37], have been derived from the absolute band intensities reported in Tables 1 and 2 of Ref. [53] by applying Eq. (A.8) and calculating the vibrational factors W_{ab} for all the fundamentals and for some overtone and combination bands. The results of such derivation are reported in Table A.10. The intensity perturbations produced by the various resonances have been taken automatically into account by the SPCAT program.

Note that the following points should be taken into account in doing this calculation:

---

[1]Note that a typo is present in Eq. (25) Ref. [54]. The correct formula for the $P(J)$ Hönl–London factors is reported in Eq. (13) of the same paper.

i. In Ref. [53] it is assumed that $\gamma_i = 1$ for all vibrational bands belonging to the same band system.

ii. The S_V^{BS} value reported for the ν_4 band is most likely to be the sum of ν_4 and $\nu_5 + \nu_7$ bands (in fact, the same feature was assigned as $\nu_5 + \nu_7$ by Khlifi et al. [63]). These two bands are very weak and separated by only $\sim 24\,\mathrm{cm}^{-1}$, so that the R branch of ν_4 completely overlaps with the P branch of $\nu_5 + \nu_7$. Based on our high-resolution measurements, we have estimated a relative intensity ratio $\nu_4{:}(\nu_5 + \nu_7)$ of 1:1.4 The reported value of $0.68\,\mathrm{cm}^{-2}\,\mathrm{atm}^{-1}$ [53] has been then split between these two bands, accordingly.

iii. The $v_4 = 1$, $v_5 = v_7 = 1$, and $v_6 = 2$ states are involved in the I RS (see § 4.1) and the intensity of the corresponding ν_4, $\nu_5 + \nu_7$, and $2\nu_6$ band are altered by the wave-function mixing. Hence, the direct use of the Θ_4, Θ_{57}, and Θ_{66} derived via Eq. (A.8) and experimental intensity data would lead to incorrect line intensity calculations. Deperturbed values ($\Theta_4^\star$, $\Theta_{57}^\star$, $\Theta_{66}^\star$) of these dipole moment derivatives have been obtained via

$$\mathbf{\Theta}^\star = \mathbf{\Theta}\,\tilde{\mathbf{V}} \tag{A.15}$$

where $\mathbf{\Theta} = (\Theta_4, \Theta_{57}, \Theta_{66})$ and $\tilde{\mathbf{V}}$ is the transpose eigenvector matrix of the vibrational Hamiltonian which includes the $v_4 = 1$, $v_5 = v_7 = 1$, and $v_6 = 2$ states. The values of $\Theta_4^\star$, $\Theta_{57}^\star$, $\Theta_{66}^\star$ are also reported in Table A.10.

Table A.10: Transition moments of HC$_3$N.

band	Intensity[a]/ cm^{-2} atm^{-1}	W_{ab}	Θ_v[b]/ 10^{-2} D	
ν_1	249.4	1/2	12.05	
ν_2	40.7	1/2	5.890	
ν_3	8.0	1/2	2.73	
ν_4	0.28[c]	1/2	0.80	(1.16)
ν_5	268.6	2	14.30	
ν_6	39.0	2	6.447	
ν_7	0.73[d]	2	1.55	
$\nu_6 + \nu_7$	12.1	2	2.897	
$\nu_5 + \nu_7$	0.40[c]	2	0.75	(0.527)
$2\nu_6$	1.72	4	0.643	(0.546)

Notes:
(a) From Ref. [53] except indicated otherwise.
(b) values in parentheses denote deperturbed values.
(c) Estimated from our experimental measurements (see text).
(d) From Ref. [64].

As far as the pure rotational transition intensities are concerned, DeLeon et al. [55] reported the experimental determination of the dipole moment in the ground (μ_0=3.73172(1) D), v_7=1 (μ_7=3.7225(2) D), and v_6=1 (μ_6=3.7263(1) D) states. In order to derive a value of the dipole moment also for other excited vibrational states observed in our rotational spectra, we expressed the dipole moment as a function of the vibrational quantum numbers, $\mu_v = \mu_e - \sum_i \delta_i \left(v_i + \frac{d_i}{2}\right)$. By analogy with the usual expansion in the vibrational quantum numbers, μ_e is the equilibrium value of the dipole moment, δ_i are the expansion coefficients and d_i the degeneracy of the i-th vibrational mode. In this fashion, a prediction of the dipole moment could be calculated from the experimental values available for all vibrational states which involve excitation of ν_6 and/or ν_7. For example, $\mu_{67} = \mu_6 + \mu_7 - \mu_0 = 3.71708$ D and $\mu_{7777} = 4\mu_7 - 3\mu_0 = 3.69484$ D. Other dipole moments that could not be derived from the experimental information were fixed to the ground state

value. This is clearly not correct but we estimated that the error introduced is in general well below 1% of the value of the dipole moment. Ultimately, the final test of the goodness of the intensity predictions was achieved by plotting the calculated spectrum against the experimental one. The consistency of the relative intensity of the infrared bands and rotational transitions confirmed the accuracy of our derivations.

References

[1] B. Turner, Detection of interstellar cyanoacetylene, Astrophys. J. 163 (1971) L35.

[2] M. J. Mumma, S. B. Charnley, The chemical composition of comets—emerging taxonomies and natal heritage, Ann. Rev. Astron. Astrophys. 49 (2011) 471–524.

[3] R. Mauersberger, C. Henkel, L. Sage, Dense gas in nearby galaxies. III- HC_3N as an extragalactic density probe, Astron. Astrophys. 236 (1990) 63–68.

[4] V. Kunde, A. Aikin, R. Hanel, D. Jennings, W. Maguire, R. Samuelson, C_4H_2, HC_3N and C_2N_2 in Titan's atmosphere, Nature 292 (5825) (1981) 686–688.

[5] N. Yu, J.-J. Wang, J.-L. Xu, Chemical evolution of HC_3N in dense molecular clouds, Mon. Not. R. Astron. Soc. 489 (2019) 4497–4512. doi:10.1093/mnras/stz2431.

[6] V. Rivilla, L. Colzi, F. Fontani, M. Melosso, P. Caselli, L. Bizzocchi, F. Tamassia, L. Dore, DC_3N observations towards high-mass star-forming regions, Mon. Not. R. Astron. Soc. 496 (2) (2020) 1990–1999.

[7] A. E. Thelen, C. A. Nixon, N. J. Chanover, M. A. Cordiner, E. M. Molter, N. A. Teanby, P. G. J. Irwin, J. Serigano, S. B. Charnley, Abundance measurements of titan's stratospheric HCN, HC_3N, C_3H_4, and CH_3CN from ALMA observations, Icarus 319 (2019) 417–432. doi:10.1016/j.icarus.2018.09.023.

[8] P. B. Rimmer, L. Majumdar, A. Priyadarshi, S. Wright, S. Yurchenko, Detectable abundance of cyanoacetylene (HC_3N) predicted on reduced nitrogen-rich super-earth atmospheres, arXiv preprint arXiv:2107.13097 (2021).

[9] J. R. Pardo, J. Cernicharo, J. R. Goicoechea, T. G. Phillips, The Slowly Expanding Envelope of CRL 618 Probed with HC_3N Rotational Ladders, Astroph. J. 615 (1) (2004) 495–505. doi:10.1086/424379.

[10] F. Rico-Villas, J. Martín-Pintado, E. González-Alfonso, V. M. Rivilla, S. Martín, S. García-Burillo, I. Jiménez-Serra, M. Sánchez-García, Vibrationally excited HC_3N emission in NGC 1068: tracing the recent star formation in the starburst ring, Mon. Not. R. Astron. Soc. 502 (2) (2021) 3021–3034. doi:10.1093/mnras/stab197.

[11] L. Bizzocchi, F. Tamassia, J. Laas, B. M. Giuliano, C. Degli Esposti, L. Dore, M. Melosso, E. Canè, A. Pietropolli-Charmet, H. S. P. Müller, H. Spahn, A. Belloche, P. Caselli, K. M. Menten, R. T. Garrod, Rotational and high-resolution infrared spectrum of HC_3N: global ro-vibrational analysis and improved line catalog for astrophysical observations, Astrophys. J. Suppl. S. 233 (2017) 11(20pp). doi:10.3847/1538-4365/aa9571.

[12] P. D. Mallinson, J. Fayt, High resolution infra-red studies of HCCCN and DCCCN, Mol. Phys. 32 (1976) 473–485. doi:10.1080/00268977600103231.

[13] F. Winther, S. Klee, G. Mellau, S. Naïm, L. Mbosey, A. Fayt, The ν_1 band system of H–CC–CN (Cyanoacetylene), J. Mol. Spectrosc. 175 (1996) 354–362. doi:10.1006/jmsp.1996.0040.

[14] K. Yamada, R. Best, G. Winnewisser, A. W. Mantz, Diode laser spectrum of HCCCN: CN stretching band, Z. Naturforsch. 38a (1983) 1296–1308. doi:10.1515/zna-1983-1205.

[15] K. Yamada, R. Schieder, G. Winnewisser, A. W. Mantz, Diode laser spectrum of HCCCN near 5 μm, Z. Naturforsch. 35a (1980) 690–693. doi:10.1515/zna-1980-0705.

[16] K. Yamada, G. Winnewisser, Diode laser spectrum of HCCCN near 5 μm. The hot band, Z. Naturforsch. 36a (1981) 23–29. doi:10.1515/zna-1981-0105.

[17] A. Dargelos, C. Pouchan, CCSD(T)-F12 calculations of the IR spectrum of cyanoacetylene HC_3N beyond the harmonic approximation, Chem. Phys. Lett. 754 (2020) 137746. doi:10.1016/j.cplett.2020.137746.

[18] R. M. Vichietti, R. L. A. Haiduke, The infrared fundamental intensities of some cyanopolyynes, Spectrochim. Acta A 90 (2012) 1–11. doi:10.1016/j.saa.2012.01.005.

[19] T. A. Holme, J. S. Hutchinson, SCF calculation of the structure, force field, and dipole function of cyanoacetylene, Chem. Phys. 93 (1985) 419–423. doi:10.1016/0301-0104(85)87006-3.

[20] J. S. Hutchinson, High-energy vibrational state of cyanoacetylene - variational and perturbative analysis of an anharmonic normal mode, J. Chem. Phys. 82 (1985) 22–30. doi:10.1063/1.448795.

[21] P. Botschwina, B. Schulz, M. Horn, M. Matuschewski, Ab initio calculations of stretching vibrational transitions for the linear molecules HCN, HNC, HCCF and HC_3N up to high overtones, Chem. Phys. 190 (1995) 345–362. doi:10.1016/0301-0104(94)00350-J.

[22] P. Botschwina, Accurate equilibrium structures for small polyatomic molecules, radicals and carbenes, Molecular Physics 103 (10) (2005) 1441–1460. doi:10.1080/00268970500070116.

[23] N. Jiang, M. Melosso, F. Tamassia, L. Bizzocchi, L. Dore, E. Canè, D. Fedele, J.-C. Guillemin, C. Puzzarini, High-resolution infrared spectroscopy of DC_3N in the stretching region, Front. Astron. Space Sci. 8 (2021) 29.

[24] M. Melosso, L. Bizzocchi, A. Adamczyk, E. Cané, P. Caselli, L. Colzi, et al., Extensive ro-vibrational analysis of deuterated-cyanoacetylene (DC_3N) from millimeter-wavelengths to the infrared domain, J. Quant. Spectrosc. Ra. 254 (2020) 107221.

[25] J.-B. Brubach, L. Manceron, M. Rouzières, O. Pirali, D. Balcon, F. Kwabia-Tchana, V. Boudon, M. Tudorie, T. Huet, A. Cuisset, P. Roy, Performance of the AILES THz-Infrared beamline at SOLEIL for high resolution spectroscopy, WIRMS 2009 AIP Conf. Proc. 1214 (2009) 81–84. doi:10.1063/1.3326359.

[26] O. Pirali, V. Boudon, J. Oomens, M. Vervloet, Rotationally resolved infrared spectroscopy of adamantane, J. Chem. Phys. 136 (2012) 024310. doi:10.1063/1.3666853.

[27] O. Pirali, M. Goubet, T. R. Huet, R. Georges, P. Soulard, P. Asselin, J. Courbe, P. Roy, M. Vervloet, The far infrared spectrum of naphthalene characterized by high resolution synchrotron FTIR spectroscopy and anharmonic DFT calculations, Phys. Chem. Chem. Phys. 15 (2013) 10151–10150. doi:10.1039/c3cp44305a.

[28] F. Matsushima, H. Odashima, T. Iwasaki, S. Tsunekawa, K. Takagi, Frequency-measurement of pure rotational transitions of H_2O from 0.5 to 5 THz, J. Mol. Struct. 352 (1995) 371–378. doi:10.1016/0022-2860(94)08531-L.

[29] V. M. Horneman, R. Anttila, S. Alanko, J. Pietila, Transferring calibration from CO_2 laser lines to far infrared water lines with the aid of the ν_2 band of OCS and the ν_2, $\nu_1 - \nu_2$, and $\nu_1 + \nu_2$ bands of $^{13}CS_2$: Molecular constants of $^{13}CS_2$, J. Mol. Spectrosc. 234 (2005) 238–254. doi:10.1016/j.jms.2005.09.011.

[30] L. Bizzocchi, M. Melosso, L. Dore, C. Degli Esposti, F. Tamassia, D. Prudenzano, V. Lattanzi, J. Laas, S. Spezzano, B. M. Giuliano, C. P. Endres, P. Caselli, Accurate Laboratory Measurement of the Complete Fine Structure of the N = 1 - 0 Transition of ^{15}NH, Astrophys. J. 863 (1) (2018) 3. doi:10.3847/1538-4357/aacffc.

[31] M. Melosso, B. Conversazioni, C. Degli Esposti, L. Dore, E. Cané, F. Tamassia, L. Bizzocchi, The pure rotational spectrum of $^{15}ND_2$ observed by millimetre and submillimetre-wave spectroscopy, J. Quant. Spectrosc. Ra. 222 (2019) 186–189.

[32] M. Melosso, L. Bizzocchi, F. Tamassia, C. Degli Esposti, E. Canè, L. Dore, The rotational spectrum of ^{15}ND. isotopic-independent Dunham-type analysis of the imidogen radical, Phys. Chem. Chem. Phys. 21 (2019) 3564–3573.

[33] L. Dore, Using fast fourier transform to compute the line shape of frequency-modulated spectral profiles, J. Mol. Spectrosc. 221 (2003) 93–98. doi:10.1016/S0022-2852(03)00203-0.

[34] R. V. Kochanov, I. Gordon, L. Rothman, P. Wcisło, C. Hill, J. Wilzewski, Hitran application programming interface (hapi): A comprehensive approach to working with spectroscopic data, J. Quant. Spectrosc. Ra. 177 (2016) 15–30.

[35] K. M. T. Yamada, F. W. Birss, M. R. Aliev, Effective Hamiltonian for polyatomic linear molecules, J. Mol. Spectrosc. 112 (1985) 347.

[36] J. M. Brown, J. T. Hougen, K.-P. Huber, J. W. C. Johns, I. Kopp, H. Lefebvre-Brion, A. J. Merer, D. A. Ramsay, J. Rostas, R. N. Zare, The labeling of parity doublet levels in linear molecules, J. Mol. Spectrosc. 55 (1975) 500.

[37] H. M. Pickett, The fitting and prediction of vibration-rotation spectra with spin interactions, J. Mol. Spectrosc. 148 (2) (1991) 371–377.

[38] K. Raghavachari, G. W. Trucks, J. A. Pople, M. Head-Gordon, A fifth-order perturbation comparison of electron correlation theories, Chem. Phys. Lett. 157 (1989) 479–483. doi:10.1016/S0009-2614(89)87395-6.

[39] A. Pietropolli Charmet, P. Stoppa, S. Giorgianni, J. Bloino, N. Tasinato, I. Carnimeo, M. Biczysko, C. Puzzarini, Accurate vibrational–rotational parameters and infrared intensities of 1-bromo-1-fluoroethene: a joint experimental analysis and ab initio study, J. Phys. Chem. A 121 (17) (2017) 3305–3317.

[40] C. Puzzarini, Accurate molecular structures of small-and medium-sized molecules, Int. J. Quantum Chem. 116 (21) (2016) 1513–1519.

[41] C. Puzzarini, V. Barone, Diving for accurate structures in the ocean of molecular systems with the help of spectroscopy and quantum chemistry, Acc. Chem. Res. 51 (2) (2018) 548–556.

[42] A. Halkier, T. Helgaker, P. Jorgensen, W. Klopper, J. Olsen, Basis-set convergence of the energy in molecular Hartree–Fock calculations, Chem. Phys. Lett. 302 (1999) 437–446. doi:10.1016/S0009-2614(99)00179-7.

[43] T. Helgaker, W. Klopper, H. Koch, J. Noga, Basis-set convergence of correlated calculations on water, J. Chem. Phys. 106 (1997) 9639–9646. doi:10.1063/1.473863.

[44] T. H. Dunning, Gaussian basis sets for use in correlated molecular calculations. I. The atoms boron through neon and hydrogen, J. Chem. Phys. 90 (1989) 1007–1023. doi:10.1063/1.456153.

[45] D. E. Woon, T. H. Dunning, Gaussian basis sets for use in correlated molecular calculations. V. Core-valence basis sets for boron through neon, J. Chem. Phys. 103 (1995) 4572–4585. doi:10.1063/1.470645.

[46] D. A. Matthews, L. Cheng, M. E. Harding, F. Lippariniand S. Stopkowicz, T.-C. Jagau, P. G. Szalay, J. Gauss, J. F. Stanton, Coupled-cluster techniques for computational chemistry: The CFOUR program package, J. Chem. Phys. 152 (2020) 214108. doi:10.1063/5.000483.

[47] J. Gauss, J. F. Stanton, Analytic CCSD(T) second derivatives, Chem. Phys. Lett. 276 (1997) 70–77. doi:10.1016/S0009-2614(97)88036-0.

[48] A. Pietropolli-Charmet, Y. Cornaton, Benchmarking fully analytic DFT force fields for vibrational spectroscopy: A study on halogenated compounds, J. Mol. Struct. 1160 (2018) 455–462. doi:10.1016/j.molstruc.2018.01.089.

[49] D. Papoušek, M. R. Aliev, Molecular vibrational-rotational spectra, Elsevier, 1982.

[50] M. R. Aliev, J. K. G. Watson, in: K. N. Rao (Ed.), Molecular Spectroscopy: Modern Research, Vol. III, Academic Press, New York, 1985, pp. 1–67.

[51] J. K. G. Watson, Higher order l-doubling of linear molecules, J. Mol. Spectrosc. 101 (1983) 83.

[52] I. E. Gordon, L. S. Rothman, R. J. Hargreaves, R. Hashemi, E. V. Karlovets, et al., The HITRAN2020 molecular spectroscopic database, J. Quant. Spectrosc. Ra. (2021) 107949doi:10.1016/j.jqsrt.2021.107949.

[53] A. Jolly, Y. Benilan, A. Fayt, New infrared integrated band intensities for HC_3N and extensive line list for the ν_5 and ν_6 bending modes, J. Mol. Spectrosc. 242 (2007) 46–54. doi:10.1016/j.jms.2007.01.008.

[54] A. Fayt, C. Vigouroux, F. Winther, Analysis of the ν_9 band complex of dicyanoacetylene and application of a theory of relative intensities to all subbands, J. Mol. Spectrosc. 224 (2) (2004) 114–130. doi:10.1016/j.jms.2004.01.004.

[55] R. L. DeLeon, J. S. Muenter, Molecular beam electric resonance study of the ground and excited states of cyanoacetylene, J. Chem. Phys. 82 (1985) 1702–1704. doi:10.1063/1.448402.

[56] I. E. Gordon, L. S. Rothman, C. Hill, R. V. Kochanov, Y. Tan, P. F. Bernath, M. Birk, V. Boudon, A. Campargue, K. Chance, et al., The HITRAN2016 molecular spectroscopic database, J. Quant. Spectrosc. Ra. 203 (2017) 3–69.

[57] G. L. Villanueva, K. Magee-Sauer, M. J. Mumma, Modeling of nitrogen compounds in cometary atmospheres: Fluorescence models of ammonia (NH_3), hydrogen cyanide (HCN), hydrogen isocyanide (HNC) and cyanoacetylene (HC_3N), J. Quant.

552   Spectrosc. Ra. 129 (2013) 158–168. `doi:10.1016/j.jqsrt.2013.06.010`.

553 [58] E. Tiesinga, P. J. Mohr, D. B. Newell, B. N. Taylor, Codata recommended values of the fundamental physical constants:
554   2018, Rev. Mod. Phys. 93 (2021) 025010(1)–025010(63). `doi:10.1103/RevModPhys.93.025010`.

555 [59] R. El Hachtouki, J. Vander Auwera, Absolute line intensities in acetylene: The 1.5-μm region, J. Mol. Spectrosc. 216
556   (2002) 355–352. `doi:0.1006/jmsp.2002.8660`.

557 [60] A. Hansson, J. K. G. Watson, A comment on Hönl-London factors, J. Mol. Spectrosc. 233 (2005) 169–173.

558 [61] J. M. Brown, A. Carrington, Rotational Spectroscopy of Diatomic Molecules, Cambridge University Press, 2003.

559 [62] G. Wagner, B. P. Winnewisser, M. Winnewisser, K. Sarka, The Infrared-Spectrum of HC^{15}NO in the Range 170–1300
560   cm^{-1}, J. Mol. Spectrosc. 162 (1993) 82.

561 [63] M. Khlifi, F. Raulin, E. Arie, G. Graner, Absolute intensity of the IR bands of propynenitrile, J. Mol. Spectrosc. 143
562   (1990) 209–211. `doi:10.1016/0022-2852(91)90085-O`.

563 [64] M. Uyemura, S. Maeda, The infrared intensities of stretching fundamentals in gaseous and crystalline cyanoacetylene,
564   Bull. Chem. Soc. Japan 47 (1974) 2930–2935. `doi:10.1246/bcsj.47.2930`.